arXiv:1410.6291v1 [astro-ph.GA] 23 Oct 2014

GLOBULAR CLUSTER SYSTEMS IN BRIGHTEST CLUSTER GALAXIES: A NEAR-UNIVERSAL LUMINOSITY FUNCTION?

William E. Harris[1], Warren Morningstar[2], Oleg Y. Gnedin[2], Heather O'Halloran[1], John P. Blakeslee[3], Bradley C. Whitmore[4], Patrick Côté[3], Douglas Geisler[5], Eric W. Peng[6], Jeremy Bailin[7], Barry Rothberg[8], Robert Cockcroft[1], and Regina Barber DeGraaff[9]
(Dated: February 26, 2018)
to be submitted to ApJ

ABSTRACT

We present the first results from our HST Brightest Cluster Galaxy (BCG) survey of seven central supergiant cluster galaxies and their globular cluster (GC) systems. We measure a total of 48000 GCs in all seven galaxies, representing the largest single GC database. We find that a log-normal shape accurately matches the observed the luminosity function (LF) of the GCs down to the GCLF turnover point, which is near our photometric limit. In addition, the LF has a virtually identical shape in all seven galaxies. Our data underscore the similarity in the formation mechanism of massive star clusters in diverse galactic environments. At the highest luminosities ($\log L \gtrsim 10^7 L_\odot$) we find small numbers of "superluminous" objects in five of the galaxies; their luminosity and color ranges are at least partly consistent with those of UCDs (Ultra-Compact Dwarfs). Lastly, we find preliminary evidence that in the outer halo ($R \gtrsim 20$ kpc), the LF turnover point shows a weak dependence on projected distance, scaling as $L_0 \sim R^{-0.2}$, while the LF dispersion remains nearly constant.

Keywords: galaxies: formation — galaxies: star clusters — globular clusters: general

1. INTRODUCTION

The luminosity function – the number of objects per unit magnitude or unit luminosity – is one of the most fundamental properties of globular cluster (GC) systems. The globular cluster luminosity function (GCLF) is the observational surrogate for the more astrophysically relevant GC *mass function* (GCMF); in turn, what we see at the present day is the product of the mass distribution of the clusters at their time of formation and the dynamical evolution of the GCs within their host galaxy over a Hubble time. In the Milky Way, either the GCLF or GCMF were long ago found to have a unimodal and nearly symmetric shape, often fit by a log-normal function (e.g., Harris 1996, 2010 edition, for the latest homogeneous collection of data).

Because the formation histories and tidal fields of galaxies can differ strongly from one another, it continues to be somewhat surprising that in galaxies of all morphological types and sizes, the GCLF has a nearly identical characteristic log-normal shape (e.g., Harris 2001a; Brodie & Strader 2006; Jordán et al. 2007). The "turnover" luminosity L_0 where the LF peaks increases weakly with galaxy mass (Jordán et al. 2007; Villegas et al. 2010). However, to first order it remains true that the turnover is so nearly universal that it can be used as a standard candle for extragalactic distance determination to a typical accuracy of a quarter-magnitude; if attention is paid to the second-order dependence of L_0 on galaxy size (Villegas et al. 2010) then the accuracy can approach ±0.15 magnitude particularly for large galaxies (see Rejkuba 2012, for a recent review).

Although in rough outline the present-day form of the GCLF is understood, quantitative details are still uncertain. Since the stellar mass-to-light ratio does not vary much with luminosity for the old stellar populations of GCs, a universal GCLF translates directly to a universal GC mass function. But a peaked distribution differs radically from the observed mass function of star clusters in nearby interacting and starbursting galaxies (e.g., Zhang & Fall 1999; Gieles 2009; Larsen 2009; Whitmore et al. 2010; Chandar et al. 2011), where extremely young clusters can be seen over a wide range of masses. This initial mass function is typically consistent with a single power law, $dN/dM \propto M^{-\beta}$ with $\beta \approx 1.8 - 2.2$ over a range of cluster mass from $10^5\,\mathrm{M}_\odot \lesssim M \lesssim 10^7\,\mathrm{M}_\odot$. Models of the dynamical evolution and disruption of GCs (e.g. Fall & Zhang 2001a; Baumgardt & Makino 2003; Gieles & Baumgardt 2008; McLaughlin & Fall 2008; Kruijssen et al. 2011, among many others) show that the fractional mass loss is strongly dependent on cluster mass; lower-mass clusters are preferentially dissolved over a Hubble time by internal evaporation coupled to the external tidal field, tidal shocking, and dynamical friction. These mechanisms seem capable of transforming an initial power-law

[1] Department of Physics & Astronomy, McMaster University, Hamilton, ON, Canada; harris@physics.mcmaster.ca, ohallohm@mcmaster.ca, cockcroft@physics.mcmaster.ca
[2] Department of Astronomy, University of Michigan, Ann Arbor, MI 48109; wmorning@umich.edu, ognedin@umich.edu
[3] Herzberg Institute of Astrophysics, National Research Council of Canada, Victoria, BC V9E 2E7, Canada;jblakeslee@nrc-cnrc.gc.ca, patrick.cote@nrc-cnrc.gc.ca
[4] Space Telescope Science Institute, 3700 San Martin Drive, Baltimore MD 21218, USA; whitmore@stsci.edu
[5] Departamento de Astronomiá, Universidad de Concepción, Casilla 160-C, Concepción, Chile; dgeisler@astroudec.cl
[6] Department of Astronomy, Peking University, Beijing 100871, China; peng@bac.pku.edu.cn
[7] Department of Physics and Astronomy, University of Alabama, Box 870324, Tuscaloosa, AL 35487-0324, USA; jbailin@ua.edu
[8] LBT Observatory, University of Arizona, 933 N.Cherry Ave, Tucson AZ 85721, USA; dr.barry.rothberg@gmail.com
[9] Department of Physics and Astronomy, Western Washington University, Bellingham WA 98225, USA; Regina.BarberDeGraaff@wwu.edu

MF into a log-normal one dominated by the highest-mass clusters, at least over the mass range that covers most clusters. Above a few $10^5 M_\odot$, however, mass loss rates are relatively slow and such massive clusters should more nearly preserve the initial MF shape.

Current attempts to incorporate the formation and evolution of GCs in the hierarchical framework of galaxy formation have had some reasonable initial success at reproducing not only the observed GCMF but also the cluster metallicity distribution in the Milky Way (Muratov & Gnedin 2010; Griffen et al. 2010) and in giant early-type galaxies (Li & Gnedin 2014). GCs are simply the most massive star clusters, and like all star clusters, they are likely to have formed as initial high-mass gaseous clumps of typically $\sim$ 1 pc scale size embedded within much more extended giant molecular clouds (GMCs) (e.g. Harris & Pudritz 1994; Burgarella et al. 2001; Bromm & Clarke 2002; Beasley et al. 2002; Shapiro et al. 2010; Elmegreen et al. 2012). Detailed cosmological simulations of the formation of high-redshift galaxies predict the existence of giant molecular clouds (GMCs) with the right large masses, sizes, and low metallicities within which embedded proto-GCs can form and eventually evolve into the extremely dense, massive GCs of the present day (Kravtsov & Gnedin 2005). A simple sub-grid model for the creation of star clusters at gas density above a fixed threshold ($10^4 \, M_\odot \, pc^{-3}$) results in a GCMF consistent with the $\beta \approx 2$ power law. Alternatively, the mass function could be described by a curved log-normal shape but with very different parameters than the present-day GCMF, motivated by the probability distribution function of clumps in a turbulent interstellar medium. Both functional forms are possible when fit over a relatively narrow range of cluster mass, but differences between them may occur at the highest cluster masses. Therefore, extending the measurement of the GCLF (and GCMF) to the most massive clusters offers the potential to test models of GC formation based on supersonic turbulence in GMCs.

Although the theoretical modelling mentioned above is more advanced than in earlier years, the numerical problem is essentially that galaxy-formation simulations must cover scales of $\sim 10^{12} M_\odot$ and ~ 100 kpc, while full resolution of proto-GCs requires resolving scales *at least* 10^7 times smaller in both quantities, an extremely steep challenge to accomplish simultaneously (see Harris 2010, for discussion). Modelling work directed at bridging this gap is ongoing (e.g. Bournaud et al. 2008; Mashchenko et al. 2008; Howard et al. 2014) but a complete theory of GC formation is not yet in hand. It is, however, globally important because a significant fraction of star formation and stellar feedback should happen in these densest, most massive clumps.

The highest-mass GCs are especially interesting as well because of their potential connections to the populations of ultra-compact dwarf galaxies (UCDs) that are typically found in rich clusters of galaxies. In structural parameter planes of effective radius, luminosity, or surface brightness the UCDs bridge the traditional gap between the GC sequence and the dwarf ellipticals (e.g. Haşegan et al. 2005; Misgeld et al. 2011; Brodie et al. 2011; Penny et al. 2014, among many others). UCDs may be especially luminous GCs, remnant nuclei of

dwarfs, remnants of multiple mergers of GCs, or genuine small-scale dwarfs. Because they are relatively rare and hard to find, their possible connections with GCs remain uncertain.

GCs with luminosities in the range $L \sim 10^4 - 10^6 L_\odot$ (i.e. the two orders of magnitude centered on the turnover luminosity) are by far the most numerous and so the shape of the GCLF is observationally well established in this middle range. The high-mass end (roughly speaking, objects like ω Centauri and above, with masses up to $10^7 M_\odot$ and beyond) is much less well surveyed. Because they are rare, very large statistical samples of GCs are needed to fill in this high-mass region.

The most effective way to accumulate the largest possible samples of GCs is through observation of the most luminous elliptical galaxies – the cD or BCG (Brightest Cluster Galaxy) systems that reside at the centers of rich galaxy clusters. Because of the empirical fact that the GCLF dispersion increases systematically with galaxy size (Villegas et al. 2010), simply stacking large numbers of smaller galaxies to gain a high$-n$ total sample is not equivalent to using a single supergiant galaxy with the same total $n(GC)$ (see, e.g., Mieske et al. 2010, for a specific example constructed from the Virgo and Fornax surveys). In the present paper, we give a brief overview of a new Hubble Space Telescope (HST) survey of GC systems in seven BCGs and discuss our first findings for the observed GCLF. In following papers of this series, we will present the complete database along with more thorough discussions of the color-magnitude diagrams, the GC metallicity distributions, and related issues relevant to the formation histories of our target galaxies.

2. BRIGHTEST CLUSTER GALAXY SURVEY

BCGs contain the most populous GC systems, but they are also a rare type of galaxy and so we must look much further afield than the closest galaxy clusters to find more than just the few that have been studied to date (Bassino et al. 2006; Harris 2009a,b; Wehner et al. 2008; Peng et al. 2011). The paradigm of a GC system in a BCG-type galaxy is that in M87, which holds 13,000 clusters (e.g. Harris 2009b). However, larger systems are known (see Harris et al. 2013), such as the Coma central cD NGC 4874 that may hold as many as 30,000 GCs (Peng et al. 2011). An even larger system may be that around Abell 1689 at $cz = 54000$ km s^{-1} (Alamo-Martínez et al. 2013). Many more BCG targets of the size of NGC 4874 or even larger have GC systems that are within reach of HST.

2.1. *Observational Material*

In this paper we present the first results of photometry for GCs in seven BCG galaxies, all of which are examples of the largest galaxies that exist in the present-day universe. Each of these was already known from previous deep ground-based imaging to contain a rich GC population (Harris et al. 1995; Bridges et al. 1996; Blakeslee et al. 1997). Our targets, listed in Table 1 in order of increasing distance, were imaged during program GO-12238 (Harris, PI) with the exception of the $F814W$ exposures for the three ESO galaxies, which came from program GO-10429 (Blakeslee, PI). The Table lists in successive columns the galaxy ID; the Abell cluster for

Table 1
Basic Parameters for BCGs in the Survey

Galaxy	Cluster	RA	Dec	$cz\,(\text{km s}^{-1})$	$(m-M)_I$	A_I	M_V^T
NGC 7720	A2634	23:38:29	+27:01:53	8714	35.61	0.107	-23.35
NGC 6166	A2199	16:28:38	+39:33:06	9125	35.60	0.017	-23.7
UGC 9799	A2052	15:16:44	+07:01:18	10500	35.95	0.056	-23.1
UGC 10143	A2147	16:02:17	+15:58:29	10741	35.99	0.047	-23.0
ESO509-G008	A1736	13:26:44	−27:26:22	10848	36.06	0.079	-23.35
ESO383-G076	A3571	13:47:28	−32:51:54	11832	36.24	0.082	-24.1
ESO444-G046	A3558	13:27:57	−31:29:44	14345	36.65	0.075	-23.8

Table 2
Parameters for the Imaging

Galaxy	F475W		F814W		R Range
	time (s)	lim mag	time (s)	lim mag	(kpc)
NGC 7720	5282	28.35	5278	27.95	12-110
NGC 6166	5370	28.5	4885	27.9	12-100
UGC 9799	7977	28.45	5253	27.77	15-105
UGC 10143	10726	28.7	5262	27.55	15-130
ESO509-G008	10758	28.65	18567	28.6	15-120
ESO383-G076	10830	28.7	21081	28.5	16-130
ESO444-G046	21660	29.25	34210	28.6	20-170

which it is the central BCG; coordinates; redshift of the galaxy cz normalized to the CBR reference frame; apparent distance modulus; foreground extinction (from NED on the Landolt scale); and $V-$band luminosity, where V_T is taken from NED. All the foreground extinctions are small and have no effect on the following analysis. Throughout the following discussion we adopt a distance scale of $H_0 = 70\,\text{km s}^{-1}\,\text{Mpc}^{-1}$. The uncertainties in the conversion to the CBR frame, and possible motion of the BCG relative to the Abell cluster center, may make the true cz differ by up to $\sim 400\,\text{km s}^{-1}$, or $0.05 - 0.10$ in distance modulus depending on distance.

The primary camera for all targets was ACS/WFC, with WFC3 being used in parallel; exposures in both cameras were through the F475W and F814W filters. In choosing these targets, to save orbits we took advantage of the long exposures in F814W of the three ESO galaxies that were already in the HST Archive. The luminosities of these giant galaxies are comparable with or even higher than the two brightest BCGs whose GC systems have previously been studied to similar depth, namely NGC 4874 in Coma and NGC 4696 in Centaurus (Harris 2009a).

In Table 2, we summarize the raw exposure data for the ACS/WFC pointings, including the total exposure times and the limiting magnitudes that resulted. Two or more orbits were used for each filter, subdivided into sequences of half-orbit exposures. The total exposures were designed to reach a limit in absolute magnitude close to the expected GCLF turnover point at $M_{V,0} \simeq -7.3$, $M_{I,0} \simeq -8.4$ and thus to secure the largest possible GC sample sizes within the limits of the program.

Preprocessing consisted of CTE correction on the raw images (Anderson & Bedin 2010), and then use of the standard Multidrizzle package to generate a combined image in each filter that kept the native pixel scale of $0.05''$.

2.2. Photometric Reductions

Photometry was carried out with the standard tools in SourceExtractor (Bertin & Arnouts 1996) and DAOPHOT (Stetson 1987) in its IRAF implementation, including aperture photometry (*phot*) and then point-spread-function (PSF) fitting through *allstar*. All PSFs were empirically generated from stars on the target fields, with anywhere from 60 to 160 individual stars on each frame. Finding bright, isolated candidate PSF stars was easily done, since our targets are all moderately high-latitude fields that are completely uncrowded in any absolute sense.

Each target galaxy was found, as expected, to be surrounded by many thousands of clusters. Virtually all of the individual GCs appear starlike: since our target systems are in the distance range $125 - 205$ Mpc, a typical GC effective radius of ~ 3 pc corresponds to an angular size in the range $0.003'' - 0.005''$, far below the $0.1''$ resolution of the telescope and safely in the "unresolved" category according to the criteria in Harris (2009a). The direct advantage for our photometry is that the GCs are therefore easily distinguished from the faint, nonstellar background galaxies that constitute the main source of sample contamination.

In the last column of Table 2, we also give the radial range $R(min) - R(max)$ from galaxy center covered by the ACS field. This $R(max)$ is determined both by the distance to the galaxy and its placement relative to the center of the ACS/WFC field of view. The innermost radii sampled for any of the galaxies are typically ~ 20 arcsec, corresponding to $R(min) \sim 10 - 20$ kpc depending on distance; at smaller radii the object detection and photometry are more severely limited by the higher surface brightness of the central galaxy. These numbers show that the bulk of our GC sample is drawn from the mid- to outer-halo regions of these supergiant galaxies.

The calibration of our data is in the VEGAMAG system, and uses the most recent filter-based zero-points given on the HST webpages to define the F475W and F814W natural magnitudes. For purposes of the present discussion, and ease of comparison with previous work (e.g. Harris et al. 2006; Harris 2009a), we use conventional (B, I) magnitudes converted from $(F475W, F814W)$ defined by the transformations in Saha et al. (2011). Using the reddening corrections for each galaxy from the NED database (listed in Table 1),

we convert the preliminary color-magnitude distributions to absolute magnitude M_I and intrinsic color $(B - I)_0$.

Figure 1 shows the color-magnitude diagrams for all seven galaxies. The huge GC populations around each one are evident, and to first order the distributions in luminosity and color are similar. To quantify the limits of the photometry, we carried out an extensive series of artificial-star tests on every field through *daophot/addstar*. The limiting magnitudes quoted in Table 2 (not de-reddened, and in the natural filter-based VEGAMAG scale) for each field and filter are the levels at which the artificial-star tests show that the completeness of detection falls to 50%. At levels $\gtrsim 0.5$ mag brighter, the completeness approaches 100%. We find that within the radial range $R \gtrsim 20$ kpc that contains the vast majority of our measured GCs, the surface brightness of the BCG itself has fallen to low enough levels that the limiting magnitudes do not depend noticeably on R. As noted above, crowding effects are also negligible in this same radial range. It is worth noting that this situation is in strong contrast to imaging of much nearer galaxies such as the Virgo members at $d \simeq 16$ Mpc (e.g. Peng et al. 2008), where the ACS field of view covers a *maximum* radius of only $R \sim 10$ kpc and the surface brightness gradient of the central galaxy across the detector is more of a concern.

In Figure 2 we show the trend of photometric measurement uncertainties for each galaxy, plotted as a function of absolute magnitude $M_{F814W} \simeq M_I$. The exposure times were planned to yield fairly uniform limits in absolute magnitude, so these curves are similar for all galaxies in the sample. As will be seen below, the uncertainties in the $F814W$ magnitudes are $\lesssim 0.1$ mag for all levels brighter than the GCLF turnover, implying that the $\simeq 1.3-$mag intrinsic width of the GCLF is negligibly broadened by photometric scatter.

Any field contamination of the GC samples is due to sparsely distributed foreground stars and a few very small, faint unresolved background galaxies. To gauge the level of contamination we used the offset WFC3 fields, placed on relatively galaxy-free locations in the outskirts of the galaxy cluster. After the same photometric procedure, rejection of nonstellar objects, and rejection of objects with extreme colors (see below), we found that the residual contamination (and thus its effects on the measured GC luminosity functions) was negligible at any level brighter than the limiting magnitudes of the survey.

The CMDs generally show evidence for broad bimodal or multimodal distributions in the GC colors. More extensive discussion will be given in following papers that concentrate on the color-magnitude and spatial distributions.

3. THE LUMINOSITY FUNCTION

3.1. *GCLF fitting*

To reduce contamination of our sample, we select only objects within the dereddened color range $1.0 < (B - I)_0 < 2.5$. A cutoff at the blue end eliminates any objects bluer than the minimum metallicity known for GCs ([Fe/H] < -2.5) (see Harris 2009a). Translation from $(B-I)_0$ to metallicity [Fe/H] here assumes the linear relation $(B-I)_0 = 2.158 + 0.375$[Fe/H] (Harris et al. 2006).

The red-end cut is based on empirical increase of contaminants in the parallel background fields, which are more frequent at colors redder than the GC sequences. In the case of ESO444, we have also cross-correlated our objects with the catalog of nucleated dwarf galaxies identified by John Blakeslee in program GO-10429. We found only 4 objects in common and eliminated those. The $0.02''$ angular resolution limit above which we could reliably identify nonstellar objects (see Harris 2009a) corresponds to a linear resolution of ~ 20 pc at the average distance of our BCG targets. This limit is not low enough to distinguish many or most UCDs from luminous GCs, so our sample is likely to include some UCDs at the high$-L$ end (see the discussion in Section 4 below).

Figure 3 shows the resulting GCLFs for each of the seven BCGs. At the lowest plotted luminosity, $L_I = 10^5 \, L_\odot$ (which is closely similar to the fiducial GCLF turnover luminosity), three systems are complete to at least 50% at that level and the others are essentially complete to $\sim 100\%$.

We fit a log-normal (Gaussian in $\log L$) distribution to the GCLF in the I-band

$$\frac{dN}{d \log L} = N_0 \exp \left[-\frac{(\log L - \log L_0)^2}{2 \sigma_L^2} \right], \qquad (1)$$

for clusters within a chosen range $L_{\min} < L_I < L_{\max}$ described below. (NB: by log we denote logarithm base-10.) To convert M_I to L_I we adopt $M_I(\odot) = 4.08$. The two free parameters are the turnover (peak) luminosity L_0 and the Gaussian dispersion σ_L, while N_0 is constrained by the total number of clusters.

We bin the data evenly spaced in $\log L$ and for consistency, we use the same bin size for all seven systems in the survey. We have experimented with varying the bin size from 0.01 dex to 0.1 dex and calculated the average χ^2 per number of degrees of freedom ($n_{\rm dof}$) of individual galaxy fits. It is defined as

$$\chi^2 = \sum_i \frac{(N_{i,\rm obs} - N_{\exp}(L_i | L_0, \sigma_L, N_0))^2}{(\Delta N_{i,\rm obs})^2}, \qquad (2)$$

where $N_{i,\rm obs}$ is the observed and completeness-corrected number of clusters in bin i, $N_{\exp}$ is the expected number from the fitting function above, and $\Delta N_{i,\rm obs} = N_{i,\rm obs}^{1/2}$ is the Poisson counting uncertainty. The number of degrees of freedom is the number of bins minus 3, accounting for L_0, σ_L, and N_0. The minimum $\chi^2/n_{\rm dof}$ occurs at $\delta \log L = 0.02$ dex, which we adopt for our analysis. This choice also results in a statistically optimum number of bins $\approx N_{\rm tot}^{1/2}$.

Limiting the range of luminosity for constraining the fit parameters is necessary because at low L the cluster counts are incomplete in both B and I, and at high L the log-normal function does not account for any superluminous clusters that form an extended tail to the LF (see Section 4 below). We have varied $\log L_{\min}$ (in Solar units) from 5.0 to 5.3 in steps of 0.1, and calculated $\chi^2/n_{\rm dof}$ for each system. Values of 5.1 and 5.2 gave similar fits for most galaxies, and therefore, we adopt $\log L_{\min} = 5.1$ to include more clusters in our analysis. This limit is also conservatively brighter (by about 1 magnitude) than the $I-$band completeness limit of the photometry, but is near the $B-$band limit for the reddest
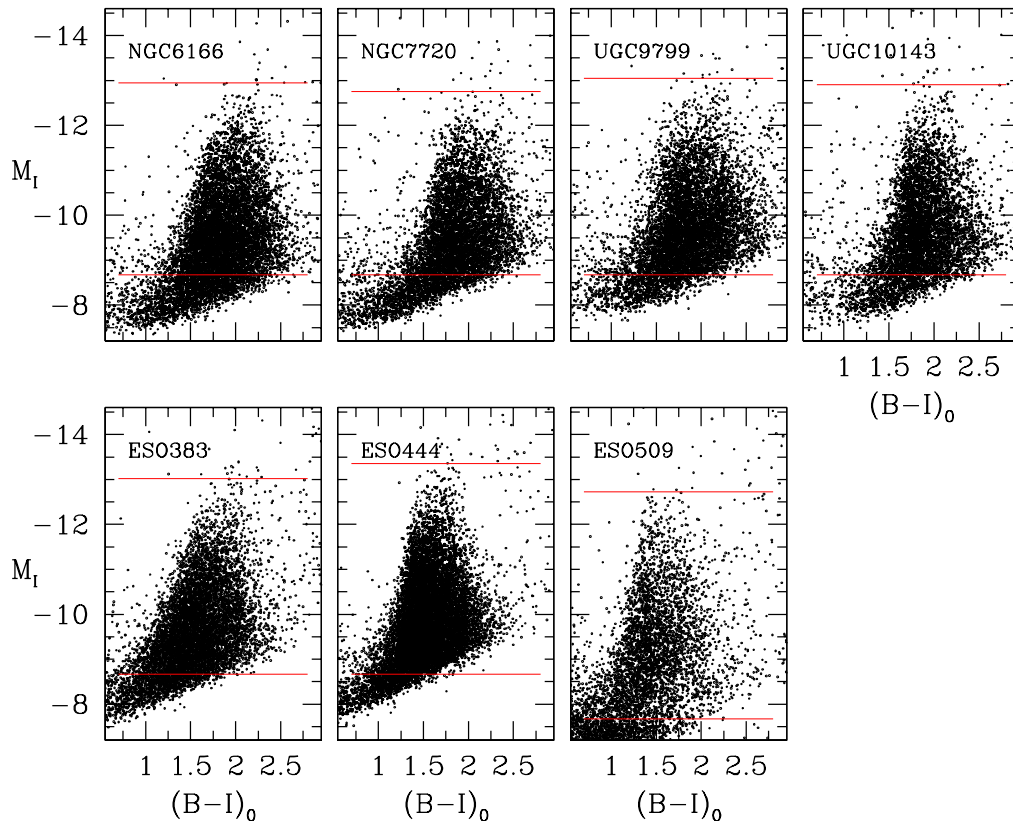
Figure 1. Color-magnitude diagrams for the seven BCGs in our sample. The filter-based magnitudes ($F475W$, $F814W$) have been converted to (B, I) as described in the text, and intrinsic colors and absolute magnitudes are calculated from the distance moduli and reddenings in Table 1. For comparison, the horizontal lines in each panel show the values of L_{min} and L_{max} within which the Gaussian LF fitting was done. The "superluminous" objects discussed in Section 4 of the text are ones brighter than L_{max}.

GCs. For one system (ESO509), we found that lowering $\log L_{\min}$ to 4.7 gave the most robust fit.

The upper $L_{\max}$ to the fitted range is determined by an iterative procedure. First, we set $L_{\max} \to \infty$ and find the best-fitting log-normal function for all clusters above $L_{\min}$. Given this fit, we define $L_{\max}$ as the limit above which the integrated GCLF predicts only 10 clusters:

$$\int_{L_{\max}}^{\infty} \frac{dN_{\exp}}{dL}\, dL = 10. \qquad (3)$$

The number 10 was chosen based on empirical comparison with the high-L tail of the observed GCLF so that small-number statistics in the uppermost L−bins would not unduly influence the fit. Integration of Equation (1) gives an explicit non-linear relation for $L_{\max}$:

$$N_0\, \sigma_L\, \sqrt{\frac{\pi}{2}}\, \mathrm{erfc}\left(\frac{\log L_{\max} - \log L_0}{\sqrt{2}\, \sigma_L} \right) = 10. \qquad (4)$$

For a given combination (L_0, σ_L, N_0), we solve this equation numerically and use the new value of $L_{\max}$ to repeat the GCLF fit. This process is iterated until $L_{\max}$ varies by less than 1%. The values of $L_{\max}$ are determined for each system individually. Clearly $L_{\max}$ is not a fixed boundary because it will be higher for galaxies with

larger total populations N_0. However, defining it this way ensures that we will be fitting the fiducial Gaussian function over the luminosity range where the number of clusters per bin is satisfactorily large. In Fig. 1 we show the adopted L_{min} and L_{max} levels for each galaxy.

The best-fit parameters (L_0, σ) for individual fits to each GC system are listed in Table 3. The 68%-confidence errorbars, $\Delta \log L_0$ and $\Delta \sigma_L$, are calculated at $\Delta \chi^2 = 1$. The table also lists the de-reddened 50% completeness limits $L_{I,\mathrm{lim}}$, which are fainter than our adopted lower cut for all systems. The fraction of missing (undetected) clusters between L_{min} and the peak of the GCLF, L_0, relative to that expected from the fit, ranges between 18% and 29%. We conclude that our samples are complete enough in the chosen luminosity range for accurate fitting to be carried out.

The observed number of clusters above the peak (shown in the second column in the table) can be roughly doubled to estimate the total expected population of the GC system, assuming the log-normal GCLF is symmetric. The total number of clusters per galaxy therefore ranges from about 6,000 to over 14,000. The currently detected number of GCs above the 50% completeness limit for all seven systems is 47,910 and the number of clusters above $L_I = 10^5\, \mathrm{L}_\odot$ is 43,783. This sample repre-
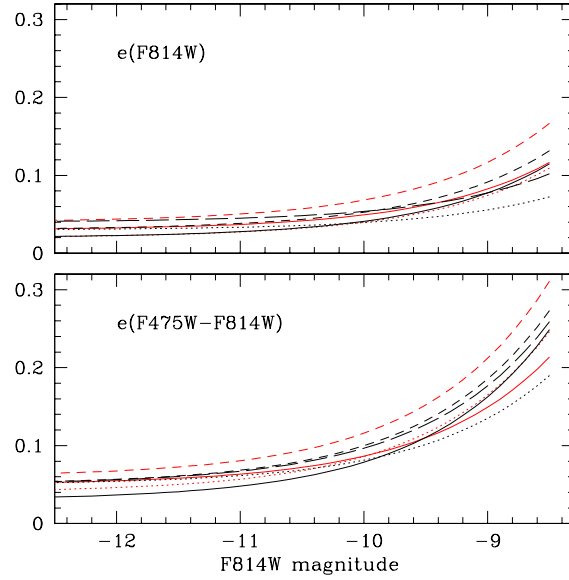
Figure 2. Measurement uncertainties in magnitude $F814W$ and color ($F475W - F814W$), plotted as a function of absolute $I-$band magnitude. *Solid red line:* NGC 6166. *Dotted red line:* NGC 7720. *Dashed red line:* UGC 9799. *Solid black line:* UGC 10143. *Dotted black line:* ESO509. *Dashed black line:* ESO383. *Dot-dashed black line:* ESO444.

Table 3
LUMINOSITY FUNCTION PARAMETERS

Galaxy	$N(L_I > L_0)$	N_{SL}	$\log L_{\max}$	$\log L_{I,\lim}$	$\log L_0$	$\Delta \log L_0$	σ_L	$\Delta\sigma_L$	$\chi^2/(n_{\mathrm{dof}})$	$\chi^2_{\mathrm{g}}/(n_{\mathrm{dof}})$	$P_{\mathrm{KS,g}}$
NGC 7720	4372	16	6.73	4.7	5.15	0.04	0.52	0.02	105/(79)	121/(74)	0.011
NGC 6166	6043	10	6.81	4.7	5.09	0.04	0.55	0.02	96/(83)	119/(78)	0.0007
UGC 9799	4765	18	6.85	4.9	5.26	0.02	0.51	0.01	74/(85)	69/(80)	0.91
UGC 10143	3674	24	6.79	5.0	5.25	0.03	0.52	0.02	83/(82)	77/(77)	0.29
ESO509-G008	2857	18	6.72	4.6	5.07	0.03	0.58	0.02	116/(99)	97/(75)	0.86
ESO383-G076	5217	29	6.84	4.7	5.30	0.02	0.49	0.01	93/(84)	74/(79)	0.72
ESO444-G046	7083	24	6.97	4.8	5.34	0.02	0.49	0.01	165/(91)	115/(86)	0.023
All (global fit)			7.14		5.24	0.01	0.52	0.01	204/(100)		

NOTES: (a) N_{SL} is the observed number of "superluminous" objects with $L_I > L_{\max}$. (b) $L_{\max}$ is the luminosity above which the log-normal fit predicts 10 clusters (see text). (c) $L_{I,\lim}$ is the 50% completeness limit. (d) L_0, σ_L, and χ^2 of the log-normal fit are calculated in the luminosity range from $10^{5.1}$ L$_\odot$ to $L_{\max}$, with the individual value of $L_{\max}$ for each galaxy. (e) χ^2_{g} and $P_{\mathrm{KS,g}}$ of the global fit are calculated over the range $L_0 - L_{\max}$.

sents the largest single dataset of GCs in the literature, an order of magnitude larger, for example, than the total number of GCs brighter than the turnover in the Virgo survey (Jordán et al. 2007).

Table 3 also lists the χ^2 of the Gaussian fit and the number of degrees of freedom, n_{dof}. For each system, the ratio of the two is between 0.87 and 1.8, which indicates that the log-normal is an appropriate fitting function for these largest GC systems.

The values of peak luminosity and the width for the seven systems are remarkably similar to each other; un-weighted direct means of the two quantities are $\langle \log L_0 \rangle = 5.21 \pm 0.04$ and $\langle \sigma_L \rangle = 0.52 \pm 0.01$. The observed rms scatter in $\log L_0$ is ± 0.10 dex; the expected $\sim 0.03-$dex scatter due simply to distance uncertainties (see Section

2 above) does not contribute significantly to that. In short, we have no evidence that the seven LFs differ systematically from each other in any major way.

To further examine this universality, we combine the clusters from all seven galaxies and perform a global log-normal fit to this combined sample. For consistency, we keep the same lower limit $L_{\min}$, but calculate $L_{\max}$ as described above. The last row of Table 3 lists the parameters of this global fit: $\log L_{0,\mathrm{g}} = 5.24$, $\sigma_{L,\mathrm{g}} = 0.52$ dex. As expected, they fall in the middle of the range for the individual systems, and are not significantly different from the unweighted mean values. The best-fit dispersion is equivalent to $\sigma_g = 1.30$ magnitudes.

Figure 4 shows the confidence intervals of the global fit parameters. As was pointed out long ago by
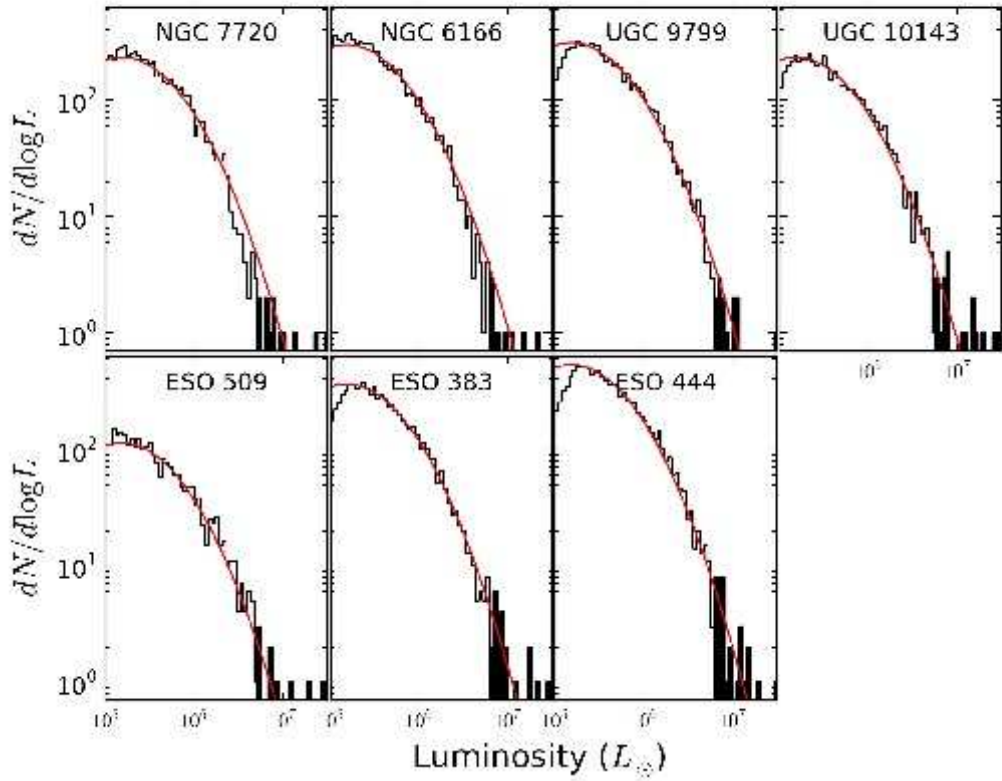
Figure 3. Luminosity function of globular cluster systems in the seven target galaxies (black histogram). Solid lines overplot the best log-normal fit for the combined global sample. Shaded parts of the histograms show super-luminous objects, defined by Equation (3). Note that in this graph, a simple power-law form for $N(L)$ would be a straight line.

Hanes & Whittaker (1987), the two parameters of the fit are partially correlated if (as is the case here) the data do not reach clearly fainter than the turnover point (the true L_0). Thus, for example, an overestimated σ leads to a fainter estimated L_0. Nevertheless, the extremely large statistical size of our database allows us to determine the parameters fairly precisely.

In the second last column of Table 3, we quantify how well this global GCLF matches each individual system by evaluating the goodness of fit $\chi^2_{\rm g}$ (without solving for the parameters separately, but simply adopting $\log L_0 = 5.24$ and $\sigma = 0.52$). The fit is calculated in the range of luminosity between $L_{0,\rm g}$ and each galaxy's $L_{\max}$. We find that the quality of the global fit is scarcely worse than the fits optimized to each individual galaxy. Lastly, we also perform a Kolmogorov-Smirnov (KS) test and calculate the probability $P_{KS,\rm g}$ (calculated over the same range as $\chi^2_{\rm g}$ and listed in the last column) that the observed cluster samples were drawn from the same *global* distribution. Table 3 shows that at least six systems have $P_{\rm KS,g} > 1\%$, which means they are not inconsistent with the universal GCLF. We note of course that these $P_{\rm KS,g}$−values cannot be as large as similar ones calculated one-by-one (where we would be testing only the hypothesis that each individual LF adequately matches the log-normal model). The KS probability is low for one galaxy (NGC 6166), primarily because of the somewhat steeper downturn of the LF at high luminosities.

In summary, we find that *our data for these seven galaxies are consistent with a "universal" lognormal GCLF shape for BCG-type systems.* Visually the global fit is indistinguishable from the individual fits. Red lines on Figure 3 overplot the global fit on the histograms of observed cluster numbers, adjusting only the normalization to the actual size of the GC system.

3.2. *Comparisons with Other Galaxies*

Several comparisons can be made for GCLF fits in other giant ellipticals. Peng et al. (2009), using the same $F814W$ bandpass for extremely deep HST data around M87, find $\log L_0 = 5.06 \pm 0.02$ and $\sigma_I = 0.55 \pm 0.02$ dex with an excellent fit to a log-normal model (see their Figure 8). Harris et al. (2009) studied the GCLFs of the Coma cluster galaxies and for a composite LF of five gE's found $\sigma_L = 0.59$ dex, $\log L_0 \simeq 5.0$ (transformed from the V−band), and again a good match to the log-normal model. These Coma data do not have as large a total GC sample and do not reach quite as faint in absolute magnitude as our present BCG sample, so the correlation noted above between the turnover point and dispersion may partly explain why the fitted L_0 is a bit fainter and σ_L a bit broader than we find.

The 7 BCGs studied here can be added to the trends of GCLF turnover and dispersion with host galaxy luminosity, as defined from the many lower-luminosity galaxies in Virgo and Fornax (Villegas et al. 2010). The results are shown in Figure 5. In the top panel, $M^{gc}_\star$ is the GC mass corresponding to the GCLF turnover luminosity, calculated with a stellar mass-to-light ratio from the Into & Portinari (2013) relations. For the Virgo and Fornax galaxies imaged with HST/ACS, the $(g - z)$ color index was used, whereas for the 7 BCGs the color index is $(B - I)$. The errorbars in $M^{gc}_\star$ for the BCGs

(for which only the bright half of the GCLF is measured) are inevitably larger than for the much nearer Virgo and Fornax members (for which almost the entire run of the GCLF was measured and the turnover is more precise). The trend derived by Villegas et al. (2010) is $\Delta\sigma/\Delta M_z = -0.10 \pm 0.01$; it is clear that the BCGs continue this trend smoothly upward.

The lower panel of Fig. 5 shows the same trend for the GCLF dispersion. Both parameters are plotted against galaxy stellar mass $M^{gal}_\star$, again derived from the Into & Portinari (2013) color-(M/L) relations. Again, the BCGs continue upward along very much the same trend defined by the smaller galaxies. In both panels, weighted best-fit lines are shown for an assumed linear relation (solid line) and a quadratic relation (dashed line); these are scarcely different, and in either case indicate that the BCGs belong to the same family as other, smaller galaxies.

The GCLF dispersion σ has also been measured for various giant galaxies at distances ~ 100 Mpc and beyond from SBF (surface brightness fluctuation) analysis. Though this method is not strictly comparable to fully resolved photometry of GCs, the results are consistent with the data listed above. Blakeslee et al. (1997), from a ground-based imaging survey of BCGs, determined $\langle\sigma_L\rangle = 0.57$ dex $(1.42 \pm 0.02$ mag) for 14 such galaxies with low internal uncertainties on σ. Overall, an empirical picture emerges in which the intrinsic width of the GCLF (for large galaxies) is consistently in the range $\sigma_L = 0.52 - 0.55$ dex.

3.3. *Internal Gradients with Galactocentric Distance*

We have also briefly investigated how the GCLF might change with projected galactocentric distance R. In Figure 6, the best-fit solutions for turnover luminosity L_0 and dispersion σ_L are plotted against R in kiloparsecs. For each galaxy the R−range was broken into $8-9$ rather narrow zones, a subdivision that was permitted by the very large statistical sample sizes (the relative numbers of clusters in each zone are indicated by the errorbar sizes in the upper panel of the figure). We note that although formal solutions were carried out for the regions $R \lesssim 20$ kpc, these should be given little weight: in these inner zones the numbers of clusters per bin are $\lesssim 100$ with few faint GCs, and the gradually increasing background light from the central galaxy begins to affect the limiting magnitude of the photometry particularly in the $F814W$ band.

In the range $R \gtrsim 20$ kpc the limiting magnitudes remain uniform (see discussion above) and the (L_0, σ_L) fits are more reliable. In all seven galaxies a consistent pattern for L_0 to decrease weakly with R is evident, with an estimated power-law slope $L_0 \sim R^{-0.2}$. The best-fit dispersion, however, remains nearly constant with R at $\sigma_L \simeq 0.4$. For comparison, the "global fit" for the dispersion, summing over all radii, is the somewhat larger value of $\sigma_L \simeq 0.5$. Given that L_0 shows a shallow dependence on R, the solutions within very restricted radial zones are expected to give smaller σ than the global average.

Regarding GCLF dependence on halo location, not much exists in the previous literature as a basis for comparison. In most cases the GCLF has been quoted as a single solution for the GC population over the entire

galaxy, or measured over a relatively small radial range determined by detector size so that systematic changes in R are not easy to see. In addition, few GCLF studies penetrate outward to the very large galactocentric distances that we have studied here. However, for the Milky Way, the analysis of Harris (2001b) (see particularly Fig. 40 and Table 9 there) does show a shallow outward decrease of the GCLF turnover luminosity for $R \gtrsim 6$ kpc, with a very similar dependence $L_0 \sim R^{-0.2}$ to that found for our BCGs. By contrast, Tamura et al. (2006) and Jordán et al. (2007) find little change in the turnover luminosity out to $R \sim 40$ kpc for the Virgo giant M87. Bassino et al. (2008) similarly find no strong change in L_0 over $8 - 60$ kpc for the Antlia giants NGC 3258 and 3268.

The simplest interpretation of a gradient in L_0 is a similarly shallow trend in mean GC mass, but L_0 is also influenced by other factors such as metallicity and dynamical evolution. The latter possibility seems unlikely, since dynamical evolution processes should be relatively ineffective at such enormous distances in the halo at reshaping the GCLF (Gnedin & Ostriker 1997; Fall & Zhang 2001b; Vesperini 2001). However, the shallow downward gradient may at least partly be explained as a byproduct of a metallicity gradient in the GC system. That is, in many large galaxies the mean GC metallicity decreases outward (e.g. Geisler et al. 1996; Rhode & Zepf 2004; Bassino et al. 2006; Harris 2009a,b; Liu et al. 2011). When we couple this trend with the observation that the GCLF turnover also becomes fainter in the smaller galaxies in which almost all the GCs are metal-poor (Jordán et al. 2007; Villegas et al. 2010), then we would expect to find a net decrease in L_0 going further outward into the progressively more metal-poor halo (and if this argument is correct, a steeper metallicity gradient in the GC system should go along with a steeper gradient in L_0). But for a fixed mean GC turnover *mass*, the $I-$band *luminosity* of the turnover is almost independent of metallicity (see the models of Ashman et al. 1995). A possible implication of the trend we see is therefore that the metal-richer GCs should be systematically more massive than the metal-poor ones. These issues will be discussed more completely in a later paper containing the metallicity distribution function measurements more explicitly.

As a final point in this section, we can ask how valid is the Gaussian LF model in the first place. This simple (two-parameter) and extremely well known functional form has been used as a quick and convenient descriptor of the GCLF for many decades, but it does not clearly result from any underlying physical theory for the formation and evolution of a GCS. Other simple forms have been tried, the most notable of which is probably the "evolved Schechter function" introduced by Jordán et al. (2007) to fit the GCLFs in the Virgo galaxies. Harris et al. (2009) applied it to the Coma giants as well. This function is asymmetric, and thus is preferable as a match for the *entire* luminosity range of GCLF because the GCLF is observed to decline more steeply on the faint side of the turnover L_0 than on the much more easily observable bright side. It also makes a logical link to the dynamical evolution of the GCS where an assumed initial power-law LF changes into the present-day form by preferential destruction of the lower-
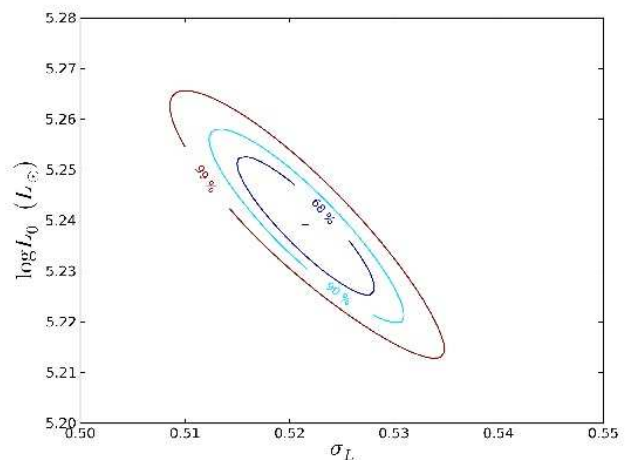

Figure 4. Confidence intervals of best-fit parameters L_0 and σ_L of a log-normal fit for the global GCLF, with all galaxies combined (Equation 1).

mass clusters (e.g. see the discussions of Vesperini 2001; Jordán et al. 2007). However, for the great majority of cases in the literature (see Harris et al. 2013, for a catalog) the range $L > L_0$ is the only part covered by the observations, and over this high-luminosity range both functions do well at matching the empirical data (see Harris et al. 2009, for a specific comparison in the Coma cluster galaxies). More importantly for the present discussion, either functional form leads to our major conclusion that the present-day GCLFs in BCG systems have a near-universal shape.

4. SUPERLUMINOUS CLUSTERS?

In addition to regular clusters well described by the log-normal function, the LFs and CMDs show a scattering of objects with luminosities of several million $L_\odot$ and above (we note here that *very* red objects are excluded by the initial color cuts). They are shown by shaded histograms at the upper tail of the distributions in Figure 3. Specifically, we adopt a working definition of superluminous objects as those with luminosities above the drop-off limit, $L > L_{\max}$. We can then assess quantitatively how likely these clusters are to appear in the sample if the true GCLF is given by our log-normal fit.

The number of superluminous clusters expected from the log-normal fit is 10, by definition of Equation (3).
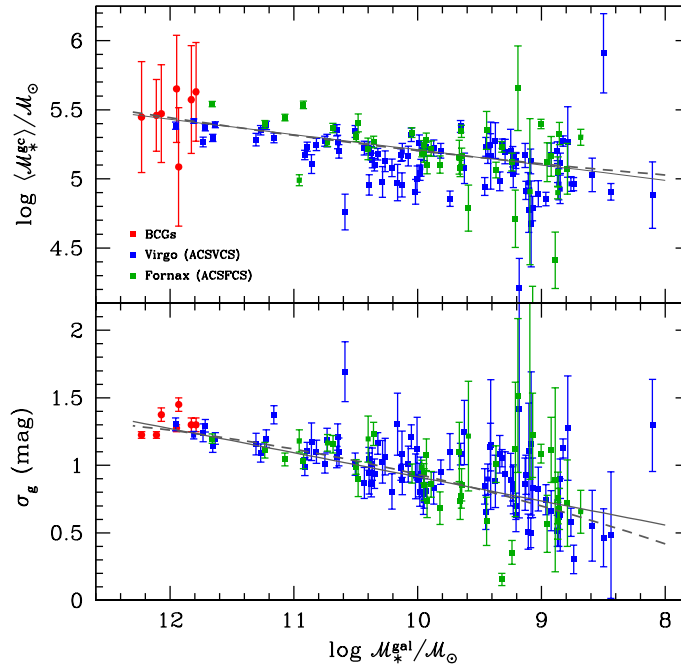
Figure 5. *Upper panel:* Correlation of GCLF turnover mass with the stellar mass of the host galaxy; here, our BCG (red points) data are added to previous measurements for the Virgo (blue points) and Fornax (green points) galaxies (Villegas et al. 2010). *Lower panel:* Correlation of the GCLF dispersion with galaxy stellar mass. In both panels, the weighted best-fit lines are shown for linear and quadratic correlations (see text).
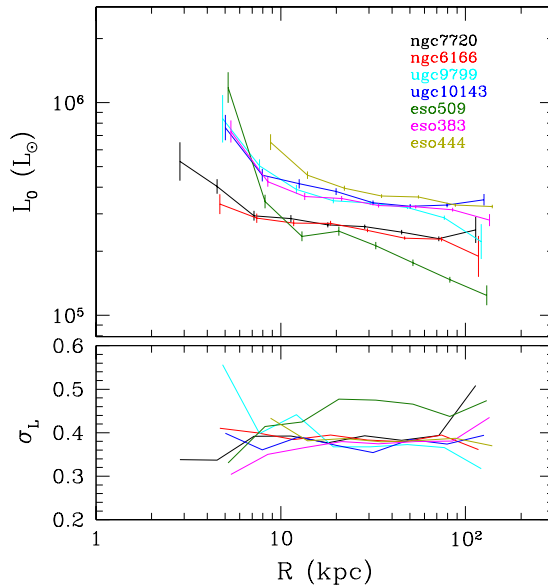

Figure 6. *Upper panel:* Correlation of the fitted GCLF turnover luminosity L_0 with projected galactocentric distance R. For $R \gtrsim 20$ kpc, L_0 scales roughly as $R^{-0.2}$ in all seven galaxies. *Lower panel:* Correlation of the fitted GCLF dispersion σ_L with projected galactocentric distance.

This will be the case *if* the LF shape continues to be strictly log-normal to arbitrarily large luminosity. But in practice, we find that only one system (NGC 6166) contains the expected number, while the other six contain "too many" superluminous clusters at the $> 2\sigma$ level if N_{SL} is governed simply by Poisson count statistics *and* if the steep dropoff in $N(L)$ at the high end follows the Gaussian-like model. The highest number is 29, in ESO383-G076. These numbers are listed as N_{SL} in Table 3.

As seen directly from the color-magnitude diagrams and the LFs in the previous figures, these objects extend up to $\sim 10^8 \, \mathrm{L_\odot}$. They *may* be the analogs of ultra-compact dwarf (UCD) galaxies, discovered in the nearby Virgo, Fornax, Hydra, Coma, and Centaurus galaxy clusters (e.g. Misgeld et al. 2011; Mieske et al. 2012). Such objects are defined as having $L \gtrsim 10^6 \, \mathrm{L_\odot}$ but otherwise are compact enough and metal-poor enough to bear some resemblances to globular clusters. As noted above, the only limits we can place on their scale sizes are that they

have effective radii $\lesssim 20$ pc, a level that would rule out only the largest UCDs.

UCDs are typically located outside of the stellar effective radius of the host galaxy. We have examined the spatial distribution of superluminous clusters and found them to be consistent with the overall location of the regular ($L < L_{max}$) clusters. The projected median distance from the host galaxy center is on the average only 20% larger for the superluminous clusters, and ranges between 2 and 4 kpc, solidly within the locus of the regular GC population.

We have also compared the color distributions of the regular and superluminous clusters for the combined sample of all seven systems. For this purpose, we adopt the lowest common luminosity threshold of $\log L_{\max} = 6.7$ to define the superluminous clusters, and to account for the vast difference in relative numbers of the two sets, we consider the cumulative fractional distributions. Figure 7 shows that the superluminous clusters are skewed systematically redder than the regular clusters; a KS test indicates that the difference between the two curves is significant well above the 99% level. In other words, the superluminous clusters tend to populate the region above the GC red sequence, though with noticeable scatter in color. Notably, the same sort of red-sequence extension was also seen in the Hydra I BCG, NGC 3311 (Wehner et al. 2008) and in the Coma BCG NGC 4874, but interestingly, *not* in the other Coma supergiant NGC 4889 (Harris et al. 2009). The brighter UCDs are also typically redder than globular clusters (Misgeld et al. 2011), arguing that at least part of this superluminous GC population may be identifiable as UCDs.

It is only in these very large BCGs, with enormous numbers of globular clusters to draw from, that we can begin seeing these small numbers of superluminous objects as forming a rough "sequence" extending upward from the bulk of the GC population (Misgeld et al. 2011). Unfortunately, gaining more information about the physical properties of the superluminous objects will be difficult, at least for the galaxies studied here. Their numbers even with this dataset are inevitably small, they are too faint ($I \sim 23, B \sim 25$) for easy spectroscopy, and spatial resolutions of $0.03''$ or less will be needed to resolve their structures with any confidence. Thus at present our case for identification of superluminous GCs with UCDs is tentative.

5. SUMMARY

We have presented the first results from a new HST imaging survey of the extremely rich globular cluster systems around BCG galaxies. The strongest conclusion from our study is that these central supergiant galaxies have GC populations that follow a remarkably similar luminosity distribution that is virtually indistinguishable from the standard log-normal shape, at least for luminosities higher than the GCLF turnover.

If we adopt a mass-to-light ratio $M/L_I \approx 2$ for the old stellar populations of GCs at an average color $(B - I)_0 \approx 1.7$, according to the empirical relations of Bell et al. (2003), then the GCLF that we observe translates into a GCMF (mass function) with the peak at $M \approx 3 \times 10^5 \, M_\odot$. The GCLF shape is strongly inconsistent with a single power-law from $10^5 \, M_\odot$ to $10^7 \, M_\odot$, contrary to what might be expected from the massive

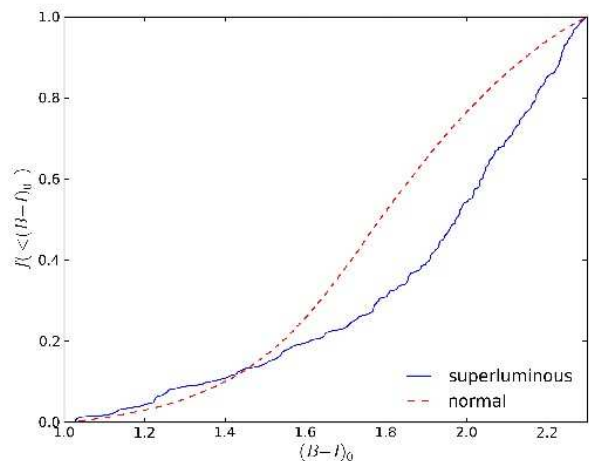

Figure 7. Cumulative distribution of the $(B - I)_0$ color of regular ($\log L < 6.7$, dashed line) and superluminous ($\log L > 6.7$, solid line) clusters for the combined sample of all seven systems. Superluminous clusters are systematically redder.

young star clusters seen in present-day merger or starburst environments. We suggest that if these massive clusters were little affected by dynamical disruption, then (at least at the high-mass end) the most massive GCs must have formed with an initial mass distribution that was not a single power-law but rather more nearly resembling a log-normal shape from the start.

In 6 of our 7 target galaxies we also find evidence for an excess of "superluminous" clusters particularly in the color range of the redder, more metal-rich GCs. Their luminosities and colors (though not their spatial distribution) provide some evidence that they may be identified as UCDs, though the case cannot be considered to be conclusive as yet.

REFERENCES

Alamo-Martínez, K. A., Blakeslee, J. P., Jee, M. J., Côté, P., Ferrarese, L., González-Lopezlira, R. A., Jordán, A., Meurer, G. R., Peng, E. W., & West, M. J. 2013, ApJ, 775, 20
Anderson, J. & Bedin, L. R. 2010, PASP, 122, 1035
Ashman, K. M., Conti, A., & Zepf, S. E. 1995, AJ, 110, 1164
Bassino, L. P., Faifer, F. R., Forte, J. C., Dirsch, B., Richtler, T., Geisler, D., & Schuberth, Y. 2006, A&A, 451, 789
Bassino, L. P., Richtler, T., & Dirsch, B. 2008, MNRAS, 386, 1145
Baumgardt, H. & Makino, J. 2003, MNRAS, 340, 227
Beasley, M. A., Baugh, C. M., Forbes, D. A., Sharples, R. M., & Frenk, C. S. 2002, MNRAS, 333, 383
Bell, E. F., McIntosh, D. H., Katz, N., & Weinberg, M. D. 2003, ApJS, 149, 289
Bertin, E. & Arnouts, S. 1996, A&AS, 117, 393
Blakeslee, J. P., Tonry, J. L., & Metzger, M. R. 1997, AJ, 114, 482
Bournaud, F., Duc, P.-A., & Emsellem, E. 2008, MNRAS, 389, L8
Bridges, T. J., Carter, D., Harris, W. E., & Pritchet, C. J. 1996, MNRAS, 281, 1290
Brodie, J. P., Romanowsky, A. J., Strader, J., & Forbes, D. A. 2011, AJ, 142, 199
Brodie, J. P. & Strader, J. 2006, ARA&A, 44, 193
Bromm, V. & Clarke, C. J. 2002, ApJ, 566, L1
Burgarella, D., Kissler-Patig, M., & Buat, V. 2001, AJ, 121, 2647
Chandar, R., Whitmore, B. C., Calzetti, D., Di Nino, D., Kennicutt, R. C., Regan, M., & Schinnerer, E. 2011, ApJ, 727, 88
Elmegreen, B. G., Malhotra, S., & Rhoads, J. 2012, ApJ, 757, 9
Fall, S. M. & Zhang, Q. 2001a, ApJ, 561, 751
—. 2001b, ApJ, 561, 751
Geisler, D., Lee, M. G., & Kim, E. 1996, AJ, 111, 1529
Gieles, M. 2009, MNRAS, 394, 2113
Gieles, M. & Baumgardt, H. 2008, MNRAS, 389, L28
Gnedin, O. Y. & Ostriker, J. P. 1997, ApJ, 474, 223
Griffen, B. F., Drinkwater, M. J., Thomas, P. A., Helly, J. C., & Pimbblet, K. A. 2010, MNRAS, 405, 375
Haşegan, M., Jordán, A., Côté, P., Djorgovski, S. G., McLaughlin, D. E., Blakeslee, J. P., Mei, S., West, M. J., Peng, E. W., Ferrarese, L., Milosavljević, M., Tonry, J. L., & Merritt, D. 2005, ApJ, 627, 203
Hanes, D. A. & Whittaker, D. G. 1987, AJ, 94, 906
Harris, W. E. 1996, AJ, 112, 1487
Harris, W. E. 2001a, in Saas-Fee Advanced Course 28: Star Clusters, ed. L. Labhardt & B. Binggeli, 223
Harris, W. E. 2001b, in Star Clusters, Saas-Fee Advanced Course 28. Lecture Notes 1998, Swiss Society for Astrophysics and Astronomy, ed. by L. Labhardt and B. Binggeli (Berlin:Springer), 223–408
—. 2009a, ApJ, 699, 254
—. 2009b, ApJ, 703, 939
—. 2010, Royal Society of London Philosophical Transactions Series A, 368, 889
Harris, W. E., Harris, G. L. H., & Alessi, M. 2013, ApJ, 772, 82
Harris, W. E., Kavelaars, J. J., Hanes, D. A., Pritchet, C. J., & Baum, W. A. 2009, AJ, 137, 3314
Harris, W. E., Pritchet, C. J., & McClure, R. D. 1995, ApJ, 441, 120
Harris, W. E. & Pudritz, R. E. 1994, ApJ, 429, 177

Harris, W. E., Whitmore, B. C., Karakla, D., Okoń, W., Baum, W. A., Hanes, D. A., & Kavelaars, J. J. 2006, ApJ, 636, 90
Howard, C. S., Pudritz, R. E., & Harris, W. E. 2014, MNRAS, 438, 1305
Into, T. & Portinari, L. 2013, MNRAS, 430, 2715
Jordán, A., McLaughlin, D. E., Côté, P., Ferrarese, L., Peng, E. W., Mei, S., Villegas, D., Merritt, D., Tonry, J. L., & West, M. J. 2007, ApJS, 171, 101
Kravtsov, A. V. & Gnedin, O. Y. 2005, ApJ, 623, 650
Kruijssen, J. M. D., Pelupessy, F. I., Lamers, H. J. G. L. M., Portegies Zwart, S. F., & Icke, V. 2011, MNRAS, 414, 1339
Larsen, S. S. 2009, A&A, 494, 539
Li, H. & Gnedin, O. Y. 2014, ApJ, submitted, arXiv:1405.0763
Liu, C., Peng, E. W., Jordán, A., Ferrarese, L., Blakeslee, J. P., Côté, P., & Mei, S. 2011, ApJ, 728, 116
Mashchenko, S., Wadsley, J., & Couchman, H. M. P. 2008, Science, 319, 174
McLaughlin, D. E. & Fall, S. M. 2008, ApJ, 679, 1272
Mieske, S., Hilker, M., & Misgeld, I. 2012, A&A, 537, A3
Mieske, S., Jordán, A., Côté, P., Peng, E. W., Ferrarese, L., Blakeslee, J. P., Mei, S., Baumgardt, H., Tonry, J. L., Infante, L., & West, M. J. 2010, ApJ, 710, 1672
Misgeld, I., Mieske, S., Hilker, M., Richtler, T., Georgiev, I. Y., & Schuberth, Y. 2011, A&A, 531, A4
Muratov, A. L. & Gnedin, O. Y. 2010, ApJ, 718, 1266
Peng, E. W., Ferguson, H. C., Goudfrooij, P., Hammer, D., Lucey, J. R., Marzke, R. O., Puzia, T. H., Carter, D., Balcells, M., Bridges, T., Chiboucas, K., del Burgo, C., Graham, A. W., Guzmán, R., Hudson, M. J., Matković, A., Merritt, D., Miller, B. W., Mouhcine, M., Phillipps, S., Sharples, R., Smith, R. J., Tully, B., & Verdoes Kleijn, G. 2011, ApJ, 730, 23
Peng, E. W., Jordán, A., Blakeslee, J. P., Mieske, S., Côté, P., Ferrarese, L., Harris, W. E., Madrid, J. P., & Meurer, G. R. 2009, ApJ, 703, 42
Peng, E. W., Jordán, A., Côté, P., Takamiya, M., West, M. J., Blakeslee, J. P., Chen, C.-W., Ferrarese, L., Mei, S., Tonry, J. L., & West, A. A. 2008, ApJ, 681, 197
Penny, S. J., Forbes, D. A., Strader, J., Usher, C., Brodie, J. P., & Romanowsky, A. J. 2014, MNRAS, 439, 3808
Rejkuba, M. 2012, Ap&SS, 341, 195
Rhode, K. L. & Zepf, S. E. 2004, AJ, 127, 302
Saha, A., Shaw, R. A., Claver, J. A., & Dolphin, A. E. 2011, PASP, 123, 481
Shapiro, K. L., Genzel, R., & Förster Schreiber, N. M. 2010, MNRAS, 403, L36
Stetson, P. B. 1987, PASP, 99, 191
Tamura, N., Sharples, R. M., Arimoto, N., Onodera, M., Ohta, K., & Yamada, Y. 2006, MNRAS, 373, 601
Vesperini, E. 2001, MNRAS, 322, 247
Villegas, D., Jordán, A., Peng, E. W., Blakeslee, J. P., Côté, P., Ferrarese, L., Kissler-Patig, M., Mei, S., Infante, L., Tonry, J. L., & West, M. J. 2010, ApJ, 717, 603
Wehner, E. M. H., Harris, W. E., Whitmore, B. C., Rothberg, B., & Woodley, K. A. 2008, ApJ, 681, 1233
Whitmore, B. C., Chandar, R., Schweizer, F., Rothberg, B., Leitherer, C., Rieke, M., Rieke, G., Blair, W. P., Mengel, S., & Alonso-Herrero, A. 2010, AJ, 140, 75
Zhang, Q. & Fall, S. M. 1999, ApJ, 527, L81